

Elevating Photooxidation of Methane to Formaldehyde via TiO₂ Crystal Phase Engineering

Yuheng Jiang

National Center for Nanoscience and Technology <https://orcid.org/0000-0002-7160-0025>

Wenshi Zhao

National Center for Nanoscience and Technology

Siyang Li

University of Chinese Academy of Sciences

Shikun Wang

University of Chinese Academy of Sciences

Yingying Fan

Guangzhou University

Fei Wang

National Center for Nanoscience and Technology

Xueying Qiu

National Center for Nanoscience and Technology

Yanfei Zhu

National Center for Nanoscience and Technology

Yin Zhang

National Center for Nanoscience and Technology

Chang Long

Molecular Electrochemistry Laboratory, Institute of Fundamental and Frontier Sciences, University of Electronic Science and Technology of China

Zhiyong Tang (✉ zytang@nanoctr.cn)

National Center for Nanoscience and Technology <https://orcid.org/0000-0003-0610-0064>

Article

Keywords: methane, photocatalytic conversion, crystal phase engineering

Posted Date: October 20th, 2021

DOI: <https://doi.org/10.21203/rs.3.rs-970368/v1>

License:  This work is licensed under a Creative Commons Attribution 4.0 International License.

[Read Full License](#)

1 **Elevating Photooxidation of Methane to**
2 **Formaldehyde via TiO₂ Crystal Phase**
3 **Engineering**

4

5 **Yuheng Jiang^{1,2,3}, Wenshi Zhao^{1,3}, Siyang Li³, Shikun Wang³, Yingying Fan⁴, Fei**
6 **Wang^{1,3}, Xueying Qiu¹, Yanfei Zhu¹, Yin Zhang¹, Chang Long^{1,5}, Zhiyong Tang¹,**
7 **3***

8

9 1 Chinese Academy of Science (CAS) Key Laboratory of Nanosystem and Hierarchy Fabrication,
10 CAS Center for Excellence in Nanoscience, National Center for Nanoscience and Technology,
11 Beijing 100190, P. R. China.

12 2 Center for Nanoscale Science and Technology, Academy for Advanced Interdisciplinary Studies,
13 Peking University, Beijing 100871, P. R. China.

14 3 University of Chinese Academy of Sciences Beijing 100049 (P. R. China).

15 4 Center for Advanced Analytical Science, School of Chemistry and Chemical Engineering,
16 School of Civil Engineering, Analytical and Testing Center, Guangzhou University, Guangzhou.

17 5 Molecular Electrochemistry Laboratory, Institute of Fundamental and Frontier Sciences,
18 University of Electronic Science and Technology of China, Chengdu, 610054, China.

19 *e-mail: zytang@nanoctr.cn

20

21 **Abstract**

22 Photocatalytic conversion of methane to value-added products under mild conditions, which
23 represents a long-sought-after goal for industrial sustainable production, remains extremely
24 challenging to afford high production and selectivity using cheap catalysts. Herein, we present the
25 crystal phase engineering of commercially available anatase TiO₂ via simple thermal annealing to
26 optimize the structure-property correlation. Biphase catalyst of anatase (90%) and rutile (10%)
27 TiO₂ exhibits the exceptional performance in the oxidation of methane to formaldehyde under the
28 reaction condition of water solvent, oxygen atmosphere and full-spectrum light irradiation. An
29 unprecedented production of 24.27 mmol g_{cat}⁻¹ with an excellent selectivity of 97.4% towards
30 formaldehyde is acquired at room temperature after a 3 h reaction. Both experimental results and
31 theoretical calculation disclose that the crystal phase engineering of TiO₂ lengthens the lifetime of
32 photogenerated carriers and favors the formation of intermediate methanol species, thus
33 maximizing the efficiency and selectivity in aerobic oxidation of methane to formaldehyde. More
34 importantly, the feasibility of scale-up production of formaldehyde is demonstrated by inventing
35 the "pause-flowing" reactor. This work opens the avenue towards industrial methane
36 transformation in a sustainable and economical way.

37

38

39

40

41

42

43

44

45

46 **Introduction**

47 Methane is the main component of natural gas and has abundant reserves on the earth¹. The
48 conversion of methane into high value-added chemicals has been always a core research topic in
49 chemistry, energy and environment fields¹⁻³. Generally, due to its intrinsic inertness of C-H bond
50 and high stability of tetrahedral structure, thermocatalytic methane conversion needs harsh
51 reaction condition⁴. As examples, conventional syngas-mediated indirect methane conversion is
52 operated at high temperatures (700°C - 1100°C); alternatively, direct partial oxidation of methane
53 could be conducted at relatively low temperature (< 200°C), but it requires strong oxidants like
54 H₂O₂ or K₂S₂O₈⁵. Distinct from the thermocatalytic systems, the photocatalysis exploits clean
55 solar energy to provide the Gibbs free energy for reaction and simultaneously generates highly
56 active free radical species, realizing the conversion of methane into value-added products
57 (methanol, formaldehyde, formic acid, ethanol, *etc.*) under mild conditions^{6, 7}. Among those
58 products, formaldehyde is highly desired since it is widely used as feedstocks in over 50 industrial
59 processes⁸. Actually, 40% of industrial methanol nowadays is employed to synthesize
60 formaldehyde^{9, 10}. Therefore, direct photocatalytic conversion of methane to formaldehyde is of
61 great significance for sustainable development.

62 Previous attempts at photooxidation of methane to formaldehyde achieved a formaldehyde
63 production of 13.1 mmol g_{cat}⁻¹ and selectivity of 86.7% over BiVO₄ nanoparticles in size of ~4.5
64 nm upon 300 nm - 400 nm irradiation for 7 h¹¹. However, the high carrier recombination rate of
65 small-sized BiVO₄ limited the further improvement of formaldehyde production. To increase the
66 carrier separation efficiency of semiconductors, loading noble metal cocatalysts is a common
67 method. Composite catalysts including Ag/ZnO¹² and Au/WO₃¹³ were applied in photooxidation
68 of methane to formaldehyde. Unfortunately, the loaded noble metal nanoparticles tended to
69 agglomerate during reaction, leading to the degradation of catalyst stability¹³. Thus, it is
70 imperative to seek the novel strategies for preparing the stable and effective photocatalysts
71 towards methane oxidation.

72 The bandgap of semiconductor photocatalysts is known to be largely dependent on the crystal
73 phase structure. For instance, the bandgap of pure anatase phase TiO₂ (denoted as A-TiO₂) and
74 rutile phase TiO₂ (denoted as R-TiO₂) is 3.2 eV and 3.0 eV, respectively¹⁴. Previous studies

75 reported that the-formed phase junction between A-TiO₂ and R-TiO₂ (A/R-TiO₂) promoted the
76 photoinduced carrier separation, thus resulting in the enhanced activity in photocatalytic water
77 splitting and pollutant degradation^{15, 16}.

78 We suppose that the crystal phase engineering of TiO₂ nanoparticles would be particularly
79 useful in photocatalytic oxidation of methane to formaldehyde. Besides the improved carrier
80 separation, the only TiO₂ utilized without introduction of additional metal cocatalysts endows the
81 chemical and photostability under the oxidation and illumination condition. We also notice that
82 beyond the catalyst construction, the adopted reactor is equally important. At present, all works
83 about the photocatalytic methane conversion have been carried out in a batch reactor, which is
84 merely suitable for small-scale catalyst screening rather than continuous production. Herein, a new
85 type of "pause-flowing" reactor is manufactured for scale-up production of formaldehyde.

86

87 **Results**

88 **Synthesis and characterization of A/R-TiO₂**

89 A/R-TiO₂ was prepared via simple thermal annealing of commercially purchased A-TiO₂
90 nanoparticles in the temperature range of 600°C to 800°C (**Fig.1a**). X-ray diffraction (XRD)
91 patterns (**Fig.1b & Fig. S1**) verify a gradual phase transition from the anatase to the rutile phase
92 with temperature increasing. The ratio of two phases is quantitatively estimated based on the
93 integrated area of rutile and anatase diffraction peaks (**Table S1**)¹⁷, and accordingly the annealed
94 samples are named as x% A-TiO₂ where x is the ratio of anatase phase inside. Analogously, the
95 Raman spectra prove that the anatase and rutile phases coexist in nanoparticles (**Fig. 1c**). The
96 characteristic peaks at 397 cm⁻¹, 515 cm⁻¹ and 637 cm⁻¹ correspond to A-TiO₂, while the peaks at
97 235 cm⁻¹, 443 cm⁻¹ and 609 cm⁻¹ belong to R-TiO₂ (**Fig. S2**)^{18, 19}. The ratio of two phases estimated
98 from Raman spectroscopy is well consistent with that obtained from the XRD patterns (**Table S2**).
99 Furthermore, high-resolution transmission electron microscopy (HRTEM) image presents the clear
100 fringe spacing of 0.352 nm and 0.325 nm, representing the anatase (101) and rutile (110) planes,
101 respectively (**Fig. 1d**)¹⁵. At the interface, the close-contacted phase junction with well-connected
102 crystal lattice is observed, which is formed through strong ionic bonds and might maximize the
103 separation efficiency of photogenerated carriers. TEM images also display that the phase transition

104 after heat treatment is accompanied by the agglomeration of TiO₂ nanoparticles, causing the
105 increase of particle size from 18 nm to 80 nm (**Fig. S3**) and the decrease of specific surface area
106 from 82 m² g⁻¹ to 35 m² g⁻¹ (**Fig. S4**).
107

108 **Energy band alignment at interfaces inside A/R-TiO₂**

109 The proper energy band structure is critical for the construction of phase junctions. The light
110 absorption ability of A/R-TiO₂ is first inspected by UV-vis diffuse reflectance spectroscopy (DRS).
111 As shown in **Fig. 2a**, A-TiO₂ and R-TiO₂ can be excited by light with wavelength below 400 nm
112 and 420 nm, respectively. As the ratio of rutile phase increasing, the absorption edge of A/R-TiO₂
113 shifts to longer wavelength, indicating that the bandgap gradually reduces. To get the optical
114 bandgap (E_g), the UV-vis DRS is transformed into a Tauc plot based on the equation $(hv\alpha)^{1/2} =$
115 A(hv - E_g), and the E_g value of A-TiO₂ and R-TiO₂ is calculated to be 3.16 eV and 2.96 eV,
116 respectively (**Fig. S5 & S6**). The Mott-Schottky and X-ray photoelectron spectroscopy (XPS)
117 valence band are further used to determine the band structure of A-TiO₂ and R-TiO₂ (**Fig. S5 &**
118 **S6**). According to the Mott-Schottky measurement, the conduction band (E_{CB}) value of A-TiO₂
119 and R-TiO₂ is -0.24 V and -0.33 V (vs NHE, NHE = normal hydrogen electrode), respectively.
120 Correspondingly, the valence band (E_{VB}) is deduced to be 2.92 V and 2.63 V (vs NHE) through the
121 formula E_{VB} = E_g + E_{CB}. In combination with the XPS valence band, the Fermi level of A-TiO₂
122 and R-TiO₂ is estimated to be 0.25 V and 0.22 V (vs NHE), respectively. **Fig. 2b** and **Table S3**
123 illustrate the detailed band structure of A-TiO₂ and R-TiO₂. The carrier transfer depends on the
124 position of the Fermi level, that is, the electrons in R-TiO₂ flow to A-TiO₂ whereas the holes in A-
125 TiO₂ flow to R-TiO₂ through the phase junction until their Fermi levels reach an equilibrium.
126 Thereafter, a built-in electric field is formed and beneficial to the separation of photogenerated
127 carriers²⁰.

128 To thoroughly clarify the effectiveness of photogenerated carrier separation at the phase
129 junction, the time-resolved transient absorption (TA) spectroscopy of A/R-TiO₂ is recorded at 355
130 nm excitation. **Fig. 2c** displays the time profiles of TA spectra probed at 600 nm. The negative
131 stimulated emission (SE) signals displayed can be fitted by the two-sided exponential function,
132 and the fitting result is summarized in **Table S4**. The short life span (τ_1) is derived from the

process of trapping excitons in the defect state, while the long life span (τ_2) reflects the recombination process of photogenerated carriers²¹. As the ratio of anatase phase in A/R-TiO₂ reduces, the τ_2 lengthens first and then shortens (top to bottom in **Fig. 2c**). Notably, the sample with an anatase ratio of 90% shows the longest lifetime (>350 ps), owning the highest efficiency of carrier separation. The difference in the separation ability of photogenerated carriers is validated by the transient photocurrent measurement (**Fig. S7**), where 90% A-TiO₂ exhibits the highest photocurrent density.

140

141 **Photocatalytic methane oxidation performance of A/R-TiO₂**

142 Based on the fact that the pipeline transportation pressure of natural gas is up to 200 bar²², high-
143 pressure reaction mode is conducive to making full use of the original energy. Moreover, a high-
144 pressure atmosphere increases the solubility of methane in water, which could boost the efficiency
145 of methane conversion²³. Thus, all the photocatalytic methane oxidation experiments have been
146 carried out in a pressured reactor at room temperature (**Fig. S8**).

147 The methane oxidation performance of 10 mg A/R-TiO₂ photocatalysts was investigated under
148 20 bar methane and 5 bar oxygen in 180 mL water with a 300 W xenon lamp irradiation (300 nm -
149 1100 nm and 130 mW cm⁻², **Fig. S9**) for 3 h. Liquid products were quantified by colorimetry for
150 formaldehyde and by NMR with water suppression pulse for others (**Fig. S10**), while gaseous
151 products were quantified by gas chromatography (GC). Control experiments manifest that the
152 presence of photocatalyst, light and methane is necessary for oxygenates production (**Table S5**).
153 As shown in **Fig. 3a & Fig. S11**, in comparison to A-TiO₂ and R-TiO₂, all A/R-TiO₂ samples
154 containing intrinsic phase junctions show a higher yield of methanol, formaldehyde and CO₂.
155 When the ratio of anatase phase is 90%, the total oxygenates production reaches the maximum
156 value, which is 5.8 and 2.3 times that of A-TiO₂ and R-TiO₂, respectively. The specific surface
157 area of nanoparticles is known to have a large influence on the photocatalytic performance²⁴, thus
158 the production is normalized by specific surface area for comparison and 90% A-TiO₂ still is of
159 the largest value (**Fig. S12a**). Besides, under the identical reaction condition, the physical mixture
160 of 90% A-TiO₂ and 10% R-TiO₂ has the total oxygenates production of 2.84 mmol g⁻¹, much
161 smaller than 10.60 mmol g⁻¹ achieved with 90% A-TiO₂ (**Fig. S12b**). These results highlight that

162 90% A-TiO₂ containing rich A/R TiO₂ phase junctions efficiently separates the photogenerated
163 carriers and thus exhibits the best photocatalytic methane oxidation performance, which is
164 consistent with TA and photocurrent measurements.

165 When the oxygen pressure is fixed at 5 bar, the total oxygenates production grows continually
166 with methane pressure increasing (**Fig. 3b**), revealing that the cleavage of methane C-H bond is
167 the rate-determining step (RDS)²⁵. It is noted that when the methane pressure exceeds 20 bar, the
168 increase rate of formaldehyde production is lower than that of methanol production (0.009 bar⁻¹ for
169 formaldehyde against 0.029 bar⁻¹ for methanol from 20 bar to 30 bar), leading to a slight drop in
170 formaldehyde selectivity (from 85.0% to 83.8%). Except for the methane pressure, the effect of
171 oxygen pressure is investigated (**Fig. 3c**). In the absence of oxygen, few oxygenates are generated.
172 When oxygen is added to the system, the oxygenates production improves dramatically and
173 reaches the plateaus at the oxygen pressure of 5 bar. After the oxygen pressure surpasses 5 bar, the
174 amount of overoxidation product CO₂ increases significantly¹¹.

175 The volume of water is also recognized as a key factor of catalytic performance (**Fig. 3d**). When
176 the photocatalytic methane oxidation reaction is carried out under anhydrous condition, only CO₂
177 is obtained. As the volume of water increases, the production of CO₂ gradually decreases
178 accompanying with formaldehyde increasing. The reason is attributed to the improved dissolution
179 of methane as well as participation of water in the desorption process of oxygenates. In addition,
180 water dilutes as-formed methanol and formaldehyde to inhibit the overoxidation process (**Fig.**
181 **S13**)¹². When the volume of water reaches 180 mL, the production of formaldehyde levels off,
182 which is limited by the active sites of catalyst and the concentration of methane.

183 To maximize the use of active sites on the surface of the nanoparticles, the mass of catalyst is
184 optimized (**Fig. 3e**). Remarkably, when 2 mg 90% A-TiO₂ is used as photocatalyst, the
185 formaldehyde production and selectivity are up to 24.27 mmol g⁻¹ and 97.36%, respectively. In this
186 reaction system, the production of methanol is too low to be detected by ¹H NMR spectroscopy
187 (**Fig. S14**), so we purposely select 10 mg 90% A-TiO₂ as standard for studying the influence of
188 varied experimental parameters on all oxidized products including methanol, formaldehyde and
189 CO₂ (**Fig. 3**). It deserves pointing out that the turnover number (TON) of oxygenates is 1.77,
190 which proves that the photooxidation of methane over 90% A-TiO₂ is a catalytic process (**Table**

191 **S6).**

192 The relationship of the photocatalytic performance with the number of photons and wavelength
193 is explored. As the light intensity increases, the production of oxygenates goes up, showing the
194 light-driven methane oxidation (**Fig. S15**). The changing trend of quantum efficiency (QE) is
195 consistent with that of the UV-vis DRS (**Fig. 3f**), and the QE is 3.28 % and 2.52 % at 313 nm and
196 365 nm, respectively (**Table S7**).

197 Altogether, the production and selectivity of formaldehyde from methane oxidation over 90%
198 A-TiO₂ upon 300 W Xenon lamp irradiation at room temperature for 3 h reaches 24.27 mmol g⁻¹
199 (or 8.09 mmol g⁻¹ h⁻¹) and 97.4%, respectively, superior to all the results achieved with the state-
200 of-the-art heterogeneous photocatalysts under similar reaction condition (**Table S8**). Furthermore,
201 the stability of 90% A-TiO₂ photocatalyst is evaluated. Prolonging the reaction time increases the
202 production of all oxygenates, but the production of CO₂ grows fastest (**Fig. S16a**), indicating that
203 a short reaction time is beneficial for avoiding overoxidation. The catalytic performance of 90%
204 A-TiO₂ remains almost stable after five cycles of reaction (**Fig. S16b**). Both XRD and XPS results
205 verify that the change of catalyst before and after the reaction is negligible, namely the ratio of
206 anatase phase in photocatalyst retains 90% (**Fig. S17**).

207

208 **Mechanism insight into activation of methane**

209 To ascertain the carbon source of liquid products, ¹³CH₄ instead of ¹²CH₄ is used as the reactant.
210 The signals at 49 ppm and 81 ppm in ¹³C composite pulse decoupling (¹³C CPD) and ¹³C 135
211 distortionless enhancement by polarization transfer (¹³C 135 DEPT) spectra are ascribed to
212 ¹³CH₃OH and HO¹³CH₂OH, respectively (**Fig. 4a**). In addition, the peaks of ¹³CH₃OH (δ = 3.08
213 ppm and 3.44 ppm) are discerned in the ¹H NMR, while the signal of ¹²CH₃OH (δ = 3.26 ppm) is
214 not detected (**Fig. S18a**). The molecular ion peak of m/z = 45 is indexed to ¹³CO₂ (**Fig. S18b**). All
215 the evidences confirm that the products originate from photocatalytic methane oxidation and
216 methane is the only carbon source.

217 As for the mechanism of methane C-H activation, the possibility of hydroxyl radical (·OH)
218 involvement is first ruled out²⁶. Fenton reaction (H₂O₂ + Fe²⁺ → Fe³⁺ + ·OH + OH⁻, pH = 4) is
219 used to replace A/R-TiO₂ based photocatalysis for ·OH generation. In this case, no product is

220 distinguished (**Table S9**), displaying that ·OH cannot activate methane in current reaction
221 condition^{12, 27}.

222 The *in situ* diffuse reflectance Fourier transform infrared spectroscopy (DRIFTS) is then
223 employed to detect the possible activation of methane on A/R-TiO₂ surface. In darkness without
224 oxygen and water, the only signal of gaseous methane (3017 cm⁻¹ and 1305 cm⁻¹) is observed,
225 showing that methane is not adsorbed on 90% A-TiO₂ surface (**Fig. S19**)²⁸. Once the light is
226 introduced, a new peak appears at 2872 cm⁻¹ which intensity increases with irradiation time
227 prolonging (**Fig. 4b & Fig. S20**). This peak is ascribed to the stretching vibration of C-H bond in
228 *CH₃O^{12, 29}. Moreover, *in situ* electron spin resonance (ESR) is utilized to probe the active species
229 produced on 90% A-TiO₂ surface (**Fig. S21**). There is no signal in darkness and dry argon
230 atmosphere, suggesting that almost no defects exist on the catalyst surface. When the light is
231 turned on, a peak of g = 2.001 appears immediately and its intensity increases gradually, which is
232 assigned to the O[·] species (hole)³⁰. Evidently, methane is activated by the lattice O[·] of 90% A-TiO₂
233 surface to generate *CH₃O species, which subsequently involves the formation of oxygenates³¹.

234 Density functional theory (DFT) calculation is adopted to understand the mechanism of
235 methane activation on A/R-TiO₂ surface. The calculated Gibbs free energy manifests that the
236 process of O[·] extracting the H atom of methane to *OCH₃ on the rutile surface has a much lower
237 energy of 0.32 eV compared to 1.18 eV on the anatase surface (**Fig. 4c & Table S10**). After
238 separating the photogenerated electrons at the phase junction, the photogenerated holes transfer to
239 the rutile surface to form lattice O[·], which is conducive to lowering the barrier of C-H bond
240 activation and promoting photocatalytic methane conversion (**Fig. 2b**). Under the anhydrous
241 condition, CO₂ is found to be the only product; after the reaction, treatment of catalyst with water
242 gives rise to the methanol generation detected by ¹H NMR, implying that the surface *OCH₃ is
243 desorbed to form methanol with the help of water (**Fig. S22**).

244

245 **Mechanism insight into aerobic oxidation of methane**

246 A contrast experiment of anaerobic oxidation of methane is carried out to uncover the role of
247 oxygen. When the reaction time is extended from 3 h to 7 h without adding O₂, the production of
248 oxygenates remains unchanged (**Fig. S23a**), indicating that the photocatalyst loses its ability to

activate methane after 3 h reaction. XPS survey is then used to assess the surface state of catalyst (**Fig. S23b**). As for pristine 90% A-TiO₂, two characteristic O 1s peaks at 529.8 eV and 531.6 eV are discerned, corresponding to the lattice oxygen (Ti-O) and the hydroxyl group (OH) adsorbed on the surface oxygen vacancies, respectively³². After the anaerobic reaction, the lattice oxygen is consumed (dropping from 92.92% to 54.02%) accompanying with generation of more oxygen vacancies (rising from 7.08% to 29.53%), which demonstrates that lattice oxygen involves in the formation of oxygenates (**Fig. S23c and Table S11**). In addition, two new peaks with the ratio of 8.40% and 8.05% appear at 532.7 eV (C-O) and 533.4 eV (C=O), corresponding to surface adsorbed methanol and formaldehyde, respectively (**Fig. S23b**)³³. The ESR spectrum of 90% A-TiO₂ after the reaction also shows a characteristic signal of oxygen vacancy at g = 2.003 (**Fig. S24**), which reinforces the consumption of lattice oxygen³⁴. As a comparison, the catalyst after the aerobic reaction has much less lattice oxygen loss (74.98%) and surface adsorbed C-O/C=O species (0%/4.9%).

The ¹⁸O isotope tracer experiment is performed to explore the reaction mechanism mediated by lattice oxygen. Owing to the low response of gas chromatography-mass spectrometry (GC-MS) method towards the main product formaldehyde, H₂¹⁸O (m/z = 20) generated by the acetylacetone color-developing reaction, where the oxygen atom of HCHO is extracted to form H₂O, is utilized to trace the isotopic HCH¹⁸O (**Fig. S10a**)¹³. When ¹⁸O₂ is used as the reactant, a distinct H₂¹⁸O (m/z = 20) signal appears via the acetylacetone color-developing reaction (**Fig. 4d**). Note that H₂¹⁸O signal is absent in the solution before the acetylacetone color-developing reaction (**Fig. S25a**). The above results disclose that ¹⁸O₂ involves in the formation of HCH¹⁸O. To judge whether the lattice oxygen of A/R-TiO₂ can be supplemented by ¹⁸O₂ (denoted as ¹⁸O-TiO₂) in the process of aerobic methane oxidation, the second round photocatalytic reaction is carried out using the recycled ¹⁸O-TiO₂ catalyst and ¹⁶O₂ reactant. The solution after the second round of catalysis is then subject to the acetylacetone color-developed reaction (**Fig. S25b**), and a clear H₂¹⁸O signal appears in the GC-MS spectrum (**Fig. 4d**). In brief, the lattice oxygen of A/R-TiO₂ participates in the formation of formaldehyde, and O₂ supplements the consumed lattice oxygen to maintain the stability of photocatalyst. Alternatively, water is another possible oxygen source in the reaction system. Similar H₂¹⁸O isotope experiments disclose that water also participates in the formation of

278 oxygenates, but it cannot supplement the lattice oxygen of photocatalyst (**Fig. S25c**).

279 After understanding the lattice oxygen determined cleavage of methane C-H bond in RDS
280 followed by methanol formation with the aid of water, another crucial question is why the
281 formaldehyde of high production and selectivity is acquired in our system. For the convenience of
282 study, methanol is directly used as the substrate instead of methane. In comparison to methane
283 reactant, the similar ratio of formaldehyde and CO₂ products is obtained with methanol substrate
284 under the identical reaction condition (**Table S12**), suggesting that methanol acts as the key
285 intermediate for the formation of formaldehyde. The *in situ* ESR experiment using 5,5-dimethyl-1-
286 pyrroline-N-oxide (DMPO) as a radical-trapping agent further shows the transformation of
287 methanol to hydroxymethyl radical (·CH₂OH, A_H = 20.5 G and A_N = 15.0 G) on A/R-TiO₂ under
288 photoirradiation (**Fig. 4e**). The ·CH₂OH radical from the reaction of methanol with hydroxyl
289 radical (·OH) is known as the intermediate for formaldehyde formation³⁵. **Fig. 4f** presents the
290 1:2:2:1 quadruple signal of hydroxyl radical generated by light irradiation. Compared with A-TiO₂
291 and R-TiO₂, the signal of hydroxyl radical is markedly enhanced on 90% A-TiO₂; meanwhile,
292 replacement of argon with oxygen in the reaction system results in 7.5 times the signal intensity of
293 hydroxyl radical (**Fig. S26**). The above results are in good agreement with the energy band
294 structure of A/R-TiO₂ (**Fig. 2b**). Namely, hydroxyl radicals are simultaneously generated by the
295 oxidation of water (·OH/H₂O = 2.380 V vs NHE) and the reduction of oxygen (O₂/H₂O₂ = 0.695 V
296 and H₂O₂/·OH = 1.14 V vs NHE). The A/R-TiO₂ phase junction promotes the separation of
297 photogenerated carriers and the generation of hydroxyl radicals, resulting in high formaldehyde
298 production and selectivity.

299 **Fig. 5** illustrates the entire process of photocatalytic aerobic oxidation of methane on A/R-TiO₂.
300 Under light irradiation, the carriers are generated inside A/R-TiO₂, where electrons in R-TiO₂ flow
301 to A-TiO₂ and holes in A-TiO₂ flow to R-TiO₂. Afterwards, methane is activated by the
302 photogenerated O[·] species mostly on the R-TiO₂ surface to form *CH₃O, which transforms to
303 methanol and then desorbs with the help of water. The O[·] species originates from the lattice
304 oxygen of TiO₂ and O₂ supplements the left oxygen vacancy of TiO₂. Finally, photogenerated
305 hydroxyl radical (·OH) from both water oxidation and oxygen reduction converts the intermediate
306 methanol in solution to formaldehyde in high yield and selectivity.

307

308 A "pause-flowing" reactor for scale-up production of formaldehyde

309 We suppose that the flowing photocatalytic system, which has a narrow optical path facilitating
310 uniform irradiation and a backpressure valve increasing the pressure of methane, will possibly
311 scale up the formaldehyde production³⁶⁻³⁸. However, the conventional continuous flowing reactor
312 employed in homogeneous photocatalysis would suffer from solid sedimentation, leading to
313 ununiform distribution or clogging of heterogeneous photocatalysts^{39, 40}. The gas-liquid-solid
314 segmented flowing system has been proved as a good solution. The flowing suspension is divided
315 into smaller subunits by the gas space, and a series of small gas-solid-liquid (G-S-L) batch
316 reactors (SMBRs) utilize the toroidal vortices in the segmented flow pattern to produce the well-
317 stirred micro-suspension containing the photocatalysts^{41, 42}.

318 Encouraged by SMBRs, a "pause-flowing" microtube reactor is designed with the unique
319 advantages of flexible control over the reaction time as well as sufficient mixing of reactants and
320 catalysts (**Fig. 6a-b & Fig. S27**). In detail, a catalyst suspension formed by A/R-TiO₂ and water
321 mixed with methane and oxygen in T-mixer generates a segmented gas-suspension flow in
322 perfluoroalkoxyalkane tube with a rich G-S-L contact interface. Next, needle valves and pressure
323 gauges are used to switch the flowing and pause modes and control the pressure of the reaction
324 system. At a pressure of 5 bar, a flow time of 15 min and a pause time of 1 h, the average
325 production of formaldehyde reaches 13.94 mmol g⁻¹ h⁻¹ L⁻¹ and its selectivity is around 100% in
326 the liquid phase, which is significantly higher than 0.26 mmol g⁻¹ h⁻¹ L⁻¹ obtained by the batch
327 reactor under the same reaction condition (**Fig. S28 & S29**). Furthermore, the stable long-term
328 production of formaldehyde is realized, which is of high potential in scale-up production (**Fig. 6c**).
329

330 Conclusion

331 Unlike the conventional heterogeneous structures that are composed of two types of different
332 materials, the phase junction in sole TiO₂ enables the efficient separation of photogenerated
333 carriers thanks to the suitable band structure alignment. More importantly, the direct chemical
334 bonding between the anatase phase and rutile phase not only maximizes the separation of
335 photogenerated carriers but also guarantees catalyst stability during photocatalytic methane

336 oxidation. These A/R-TiO₂ photocatalysts are further applied in the "pause-flowing" reactor for a
337 scale-up generation. As a result, we realize the efficient, selective, continuous and stable
338 production of formaldehyde via photocatalytic methane oxidation under mild condition. This work
339 offers a paradigm to approach the industrial photocatalytic transformation of low carbon
340 feedstocks including but not limited to methane via rational design of both catalysts and reactors.

341

342 Methods

343 **Chemicals.** Nano-TiO₂ (99.8% metals basis, 5-10 nm) was purchased from Aladdin. Hydrogen
344 peroxide aqueous solution (30% w/w) was bought from Gaoheng (Beijing). Deuterium oxide (99.9
345 atom% D) and dimethyl sulfoxide (DMSO) were obtained from Innochem. Deionized water with a
346 resistivity of 18.2 MΩ cm⁻¹ was used in all experiments. All chemicals were used as received and
347 without further purification.

348

349 **Anatase-rutile phase junction TiO₂ (A/R-TiO₂) preparation.** A/R-TiO₂ was prepared through a
350 simple thermal treatment method. 200 mg commercial nano-TiO₂ power (A-TiO₂) was calcinated
351 at different temperatures (600°C, 650°C, 700°C and 800°C) in a muffle furnace for 2 h at a heating
352 rate of 5°C/min. Finally, A/R TiO₂ with different anatase and rutile ratios was obtained. According
353 to the XRD results (**Table S1**), the anatase ratio was 100% (A-TiO₂), 90% (600°C), 70% (650°C),
354 30% (700°C) and 100% (800°C), named as A-TiO₂, 90% A-TiO₂, 70% A-TiO₂, 30% A-TiO₂ and
355 R-TiO₂, respectively.

356

357 **Characterization.** Transmission electron microscopy (TEM) imaging was carried out using
358 Tecnai G2 F20 S-TWIN at 200 kV. Powder X-ray diffraction (PXRD) data were collected on
359 D/MAX-TTRIII (CBO) with Cu K α radiation ($\lambda = 1.542 \text{ \AA}$) operating at 40 kV and 200 mA.
360 Raman spectra were recorded on Renishaw inVia plus. X-ray photoelectron spectroscopy (XPS)
361 spectra were acquired in an ESCALAB 20 Xi XPS system, where the analysis chamber was $1.5 \times$
362 10^{-9} mbar and the size of the X-ray spot was 500 μm. The binding energies were referenced to the
363 C 1s line at the binding energy of 284.8 eV from adventitious carbon. The nitrogen adsorption and
364 desorption isotherms were measured at 77 K using a Micromeritics ASAP 2020-4 system. The

365 samples were outgassed at 200°C for 2 h before measurement. Surface areas were calculated from
366 the adsorption data using Langmuir and Brunauer-Emmett-Teller (BET) methods. *In situ* electron
367 spin spectra (ESR) were detected at 9.43 GHz and room temperature using a Bruker E500
368 spectrometer. *In situ* diffuse reflectance Fourier transform infrared spectroscopy (DRIFTS) was
369 obtained by Thermo Scientific Nicolet IS50.

370

371 **Photoelectric performance measurement and energy band structure determination.** Taking
372 Al₂O₃ as the reference sample, the UV-vis diffuse reflectance spectrum (DRS) was recorded by a
373 Hitachi U-3010 UV-visible spectrometer. For the Mott-Schottky and photocurrent test, 6 mg
374 sample was ultrasonically dispersed in a mixed solution (580 μL ethanol and 20 μL 5% Nafion)
375 before it was added dropwise onto 1 * 1 cm indium tin oxide (ITO) as the working electrode.
376 Using Ag/AgCl as the reference electrode and platinum mesh as the counter electrode, the Mott-
377 Schottky plots were obtained using CHI-760E electrochemical workstation where samples in 1 M
378 Na₂SO₄ were tested at a frequency of 700 Hz; meanwhile, the photocurrent was determined at 1 V.

379

380 **Transient absorption spectroscopy**

381 The femtosecond transient absorption (fs-TA) measurements were obtained by the light
382 conversion commercial fs-TA system. Fundamental 800 nm pulse (33 kHz, 190 fs) from a
383 Coherent Astrella regenerative amplifier was used to pump an optical parametric amplifier
384 (Coherent, OperA Solo) to obtain a frequency-tunable pump beam across the visible light region.
385 The pump beam was severed and focused at the sample with a beam waist of approximately 300
386 μm. The pump light wavelength was 355 nm. A white-light continuum probe beam from 420 nm
387 to 820 nm was acquired by focusing a weak part of the fundamental 800 nm beam on a sapphire
388 window. The sample was placed in the overlapped position of the pump beam and the white-light
389 continuum probe beam. All samples in measurements were in water solution and obtained with 1
390 mm quartz cuvettes. The recovery signal was fitted by multi-exponential decay function with a
391 lifetime τ_i , convoluted by a Gaussian response function:

392

$$D(t) = y_0 + \sum A_i \exp\left(\frac{t}{\tau_i}\right) \left[1 - \operatorname{erf}\left(-\frac{t - \frac{s_0^2}{\tau_i}}{s_0}\right) \right]$$

393

394 where i was set as 3, y_0 was baseline height and s_0 was the laser pulse width. For each τ_i , its
 395 proportion p_i was calculated by $p_i = \frac{A_i \tau_i}{\sum A_i \tau_i}$. Fitting results were given in **Table S4**.

396

397 **Photocatalytic methane oxidation.** The photocatalytic methane oxidation was carried out in a
 398 stainless-steel autoclave (**Fig. S8**). The photocatalysis experiment was carried out at the given
 399 methane and oxygen pressure and room temperature (25°C). The catalyst was dispersed in a
 400 specific volume of water, which was then added to the reactor. After the reactor was sealed,
 401 methane was continuously injected for 5 min to remove the dissolved oxygen in the water. Then
 402 methane and oxygen at the given pressure were charged into the system. A xenon lamp (emission
 403 wavelength of 300 nm -1100 nm and light intensity of 130 mW cm⁻¹, PerfectLight) was used to
 404 initiate the photocatalytic reaction. In the experiments of measuring the quantum yield, bandpass
 405 filters at the corresponding wavelengths were used to obtain monochromatic light.

406

407 **Product analysis.** Analysis and quantification of CH₃OH were carried out by ¹H NMR with water
 408 suppression pulse using dimethyl sulfoxide (DMSO) as an internal standard. Typically, 0.2 mL
 409 post-reaction liquid was mixed with 0.4 mL D₂O and 0.07 μmol DMSO. The concentration of
 410 methanol standard solutions was plotted versus the corresponding area ratio to DMSO to obtain
 411 the calibration curves. The products were quantified by comparing the ¹H NMR signal against the
 412 calibration curve (**Fig. S10b**). A Shimadzu GC-MS QP2010 Ultra was used for monitoring the
 413 generation of ¹³CH₃OH, H₂¹⁸O and ¹³CO₂. The ¹H NMR, ¹³C CPD and ¹³C DEPT-135 spectra
 414 were recorded by a Bruker AVANCE III HD 400 MHz NMR spectrometer.

415 The production of HCHO in water was assessed through the acetylacetone color-developing
 416 method. A portion of the product solution (3 mL) was mixed with as-prepared 0.25% (v/v)
 417 acetylacetone solution (2 mL) before being heated for 3 min in boiling water. Through absorbance
 418 intensity detection at 413 nm against the calibration curve, the HCHO content was obtained (**Fig.**

419 **S10a & c).**

420

421 **Preparation of 0.25% (v/v) acetylacetone solution.** Ammonium acetate (25 g) was dissolved in
422 water (10 mL). Subsequently, acetic acid (3 mL) and acetylacetone (0.25 mL) were added in
423 sequence. Afterward, the solution volume was diluted with deionized water to 100 mL. With the
424 pH adjusted to 6, the solution was stored at 2°C - 5°C, at which temperature would remain stable
425 for one month.

426

427 **Computational method**

428 The Vienna Ab Initio Simulation Package (VASP) was employed to perform all the density
429 functional theory (DFT) calculations within the generalized gradient approximation (GGA) using
430 the Perdew-Burke-Ernzerhof (PBE) formulation. The projected augmented wave (PAW) potentials
431 were chosen to describe the ionic cores. Valence electrons were taken into account by using a
432 plane-wave basis set with a kinetic energy cutoff of 450 eV. Partial occupancies of the
433 Kohn–Sham orbitals were allowed using the Gaussian smearing method and a width of 0.05 eV.
434 The electronic energy was considered self-consistent when the energy change was smaller than
435 10^{-5} eV. Geometry optimization was considered convergent when the energy change was smaller
436 than 0.03 eV/Å. The Brillouin zone was sampled with $2 \times 2 \times 1$ Monkhorst mesh.

437 The free energy on the surface was calculated as follows:

438
$$\Delta G = \Delta E (\text{DFT}) + \Delta E (\text{ZPE}) - T\Delta S$$

439 where E (DFT) was the total energy for the adsorption of CH_4^* and OCH_3^* , ΔE (ZPE) was the
440 zero-point energy change and ΔS was the entropy change.

441

442 **Photocatalytic methane oxidation in “pause-flowing” reactor**

443 A schematic overview of the "pause-flowing" reactor was given in **Fig. S27**. The tube reactor was
444 constructed using perfluoroalkoxyalkane (PFA) tube (outside diameter = 3 mm, inside diameter =
445 1 mm, length = 30 m, volume = 25 mL), which was wrapped around the outer wall of a cylinder.
446 Meanwhile, near-UV LED strip (2.5 m, 365 nm, 120 W) was attached to the inner wall of hollow
447 cylinder with a larger diameter to form photobox. The above two cylinders were assembled to

448 fabricate a photoreactor. The gas flow rate (CH_4 and O_2) and CH_4/O_2 ratio ($\text{CH}_4/\text{O}_2 = 4/1$) were
449 monitored and controlled by a mass flow controller (MFC). The catalyst suspension was pumped
450 via a gear pump. All reactants including catalyst suspension, CH_4 and O_2 were mixed in a T-mixer
451 and the 1:1 gas/suspension segmented flow was introduced in the tube reactor. Two needle valves
452 were located at each end of the reactor to switch the flowing and pause modes. The pressure inside
453 the reactor was regulated by needle valves and pressure gauge to be 5 bar.

454 When the flowing mode started, valve 1 and valve 2 were opened, and the tube reactor was
455 filled by the segmented gas/suspension flow. When the set pressure reached, both valve 1 and
456 valve 2 were closed to start the pause mode. After 1 h reaction, valve 2 was opened, and the
457 mixture of suspension and product in the tube reactor automatically run down to the collector. At
458 the same time, valve 1 was opened to replace the reaction stream in the tube reactor with a new
459 segmented gas-suspension flow. After 15 min flowing, both valve 1 and valve 2 were closed again
460 to start the next round of reaction. Finally, the mixture of suspension and product in the collector
461 were separated and the resulting solution was used to quantify the production of methanol and
462 formaldehyde.

463 **References**

- 464 1. Saha, D., Grappe, H.A., Chakraborty, A. & Orkoulas, G. Postextraction Separation, On-Board
465 Storage, and Catalytic Conversion of Methane in Natural Gas: A Review. *Chem Rev* **116**,
466 11436-11499 (2016).
- 467 2. Schwach, P., Pan, X.L. & Bao, X.H. Direct Conversion of Methane to Value-Added Chemicals
468 over Heterogeneous Catalysts: Challenges and Prospects. *Chemical Reviews* **117**, 8497-8520
469 (2017).
- 470 3. Caballero, A. & Perez, P.J. Methane as raw material in synthetic chemistry: the final frontier.
471 *Chem Soc Rev* **42**, 8809-8820 (2013).
- 472 4. Yu-Ran, L. Comprehensive Handbook of Chemical Bond Energies. (CRC Press, 2007).
- 473 5. Meng, X. et al. Direct Methane Conversion under Mild Condition by Thermo-, Electro-, or
474 Photocatalysis. *Chem* **5**, 2296-2325 (2019).
- 475 6. Song, H., Meng, X.G., Wang, Z.J., Liu, H.M. & Ye, J.H. Solar-Energy-Mediated Methane
476 Conversion. *Joule* **3**, 1606-1636 (2019).
- 477 7. Yuliati, L. & Yoshida, H. Photocatalytic conversion of methane. *Chem Soc Rev* **37**, 1592-1602
478 (2008).
- 479 8. Heim, L.E., Konnerth, H. & Prechtl, M.H.G. Future perspectives for formaldehyde: pathways
480 for reductive synthesis and energy storage. *Green Chemistry* **19**, 2347-2355 (2017).
- 481 9. Bahmanpour, A.M., Hoadley, A. & Tanksale, A. Formaldehyde production via hydrogenation
482 of carbon monoxide in the aqueous phase. *Green Chemistry* **17**, 3500-3507 (2015).
- 483 10. Sam, B., Breit, B. & Krische, M.J. Paraformaldehyde and methanol as C1 feedstocks in metal-
484 catalyzed C-C couplings of pi-unsaturated reactants: beyond hydroformylation. *Angew Chem
485 Int Ed Engl* **54**, 3267-3274 (2015).
- 486 11. Fan, Y.Y. et al. Selective photocatalytic oxidation of methane by quantum-sized bismuth
487 vanadate. *Nat Sustain* **4**, 509-515 (2021).
- 488 12. Song, H. et al. Direct and Selective Photocatalytic Oxidation of CH₄ to Oxygenates with O₂ on
489 Cocatalysts/ZnO at Room Temperature in Water. *Journal of the American Chemical Society*
490 **141**, 20507-20515 (2019).
- 491 13. Wei, S.L. et al. Aerobic oxidation of methane to formaldehyde mediated by crystal-O over

- 492 gold modified tungsten trioxide via photocatalysis. *Appl Catal B-Environ* **283**, 119661-119670
493 (2021).
- 494 14. Scanlon, D.O. et al. Band alignment of rutile and anatase TiO₂. *Nat Mater* **12**, 798-801 (2013).
- 495 15. Zhang, J., Xu, Q., Feng, Z., Li, M. & Li, C. Importance of the relationship between surface
496 phases and photocatalytic activity of TiO₂. *Angew Chem Int Edit* **47**, 1766-1769 (2008).
- 497 16. Su, R. et al. How the Anatase-to-Rutile Ratio Influences the Photoreactivity of TiO₂. *J Phys*
498 *Chem C* **115**, 24287-24292 (2011).
- 499 17. Spurr, R.A. & Myers, H. Quantitative Analysis of Anatase-Rutile Mixtures with an X-Ray
500 Diffractometer. *Analytical Chemistry* **29**, 760-762 (1957).
- 501 18. Zhang, W.F., He, Y.L., Zhang, M.S., Yin, Z. & Chen, Q. Raman scattering study on anatase
502 TiO₂ nanocrystals. *J Phys D Appl Phys* **33**, 912-916 (2000).
- 503 19. Aita, C.R. Raman scattering by thin film nanomosaic rutile TiO₂. *Applied Physics Letters* **90**,
504 213112-213114 (2007).
- 505 20. Liu, F. et al. Direct Z-Scheme Hetero-phase Junction of Black/Red Phosphorus for
506 Photocatalytic Water Splitting. *Angewandte Chemie* **131**, 11917-11921 (2019).
- 507 21. Li, R. et al. Integration of an inorganic semiconductor with a metal-organic framework: a
508 platform for enhanced gaseous photocatalytic reactions. *Adv Mater* **26**, 4783-4788 (2014).
- 509 22. Kumar, S. et al. LNG: An eco-friendly cryogenic fuel for sustainable development. *Applied*
510 *Energy* **88**, 4264-4273 (2011).
- 511 23. Taylor, C.E. Photocatalytic conversion of methane contained in methane hydrates. *Top Catal*
512 **32**, 179-184 (2005).
- 513 24. Xu, Q.A. et al. Enhancing hydrogen production activity and suppressing CO formation from
514 photocatalytic biomass reforming on Pt/TiO₂ by optimizing anatase-rutile phase structure. *J*
515 *Catal* **278**, 329-335 (2011).
- 516 25. Tian, J. et al. Direct conversion of methane to formaldehyde and CO on B₂O₃ catalysts. *Nat*
517 *Commun* **11**, 5693-5699 (2020).
- 518 26. Ogura, K. & Kataoka, M. Photochemical conversion of methane. *Journal of Molecular*
519 *Catalysis* **43**, 371-379 (1988).
- 520 27. Xie, J. et al. Highly selective oxidation of methane to methanol at ambient conditions by

- 521 titanium dioxide-supported iron species. *Nature Catalysis* **1**, 889-896 (2018).

522 28. Zhou, Y., Zhang, L. & Wang, W. Direct functionalization of methane into ethanol over copper
523 modified polymeric carbon nitride via photocatalysis. *Nat Commun* **10**, 506-513 (2019).

524 29. Chen, T. et al. Mechanistic studies of photocatalytic reaction of methanol for hydrogen
525 production on Pt/TiO₂ by in situ Fourier transform IR and time-resolved IR spectroscopy. *J
526 Phys Chem C* **111**, 8005-8014 (2007).

527 30. Hurum, D.C., Agrios, A.G., Gray, K.A., Rajh, T. & Thurnauer, M.C. Explaining the Enhanced
528 Photocatalytic Activity of Degussa P25 Mixed-Phase TiO₂ using EPR. *The Journal of
529 Physical Chemistry B* **107**, 4545-4549 (2003).

530 31. Zhu, S. et al. Efficient Photooxidation of Methane to Liquid Oxygenates over ZnO Nanosheets
531 at Atmospheric Pressure and Near Room Temperature. *Nano Lett* **21**, 4122-4128 (2021).

532 32. Wang, T. et al. Synergistic Pd Single Atoms, Clusters, and Oxygen Vacancies on TiO₂ for
533 Photocatalytic Hydrogen Evolution Coupled with Selective Organic Oxidation. *Small* **17**,
534 2006255-2006264 (2021).

535 33. Li, W. et al. Selective CO Production by Photoelectrochemical Methane Oxidation on TiO₂.
536 *ACS Cent Sci* **4**, 631-637 (2018).

537 34. Hurum, D.C., Gray, K.A., Rajh, T. & Thurnauer, M.C. Recombination pathways in the
538 Degussa P25 formulation of TiO₂: surface versus lattice mechanisms. *J Phys Chem B* **109**,
539 977-980 (2005).

540 35. Xie, S. et al. Visible light-driven C-H activation and C-C coupling of methanol into ethylene
541 glycol. *Nat Commun* **9**, 1181-1187 (2018).

542 36. Xue, F. et al. Reaction discovery using acetylene gas as the chemical feedstock accelerated by
543 the "stop-flow" micro-tubing reactor system. *Chem Sci* **8**, 3623-3627 (2017).

544 37. Chen, Y. et al. Tuning the gas-liquid-solid segmented flow for enhanced heterogeneous
545 photosynthesis of Azo- compounds. *Chemical Engineering Journal* **423**, 130226-130235
546 (2021).

547 38. Guidi, M., Seeberger, P.H. & Gilmore, K. How to approach flow chemistry. *Chem Soc Rev* **49**,
548 8910-8932 (2020).

549 39. Hu, A., Guo, J.J., Pan, H. & Zuo, Z. Selective functionalization of methane, ethane, and higher

550 alkanes by cerium photocatalysis. *Science* **361**, 668-672 (2018).

551 40. Laudadio, G. et al. C(sp³)–H functionalizations of light hydrocarbons using decatungstate
552 photocatalysis in flow. *Science* **369**, 92-96 (2020).

553 41. Pieber, B., Shalom, M., Antonietti, M., Seeberger, P.H. & Gilmore, K. Continuous
554 Heterogeneous Photocatalysis in Serial Micro-Batch Reactors. *Angew Chem Int Ed Engl* **57**,
555 9976-9979 (2018).

556 42. Bajada, M.A. et al. Visible-Light Flow Reactor Packed with Porous Carbon Nitride for
557 Aerobic Substrate Oxidations. *ACS Appl Mater Interfaces* **12**, 8176-8182 (2020).

558

559

560 **Acknowledgements**

561 The authors acknowledge financial support from the Strategic Priority Research Program of
562 Chinese Academy of Sciences (XDB36000000, Z.Y.T.), National Key Basic Research Program of
563 China (2016YFA0200700, Z.Y.T.), National Natural Science Foundation of China (92056204,
564 21890381 and 21721002, Z.Y.T.), and Frontier Science Key Project of Chinese Academy of
565 Sciences (QYZDJ-SSW-SLH038, Z.Y.T.).

566

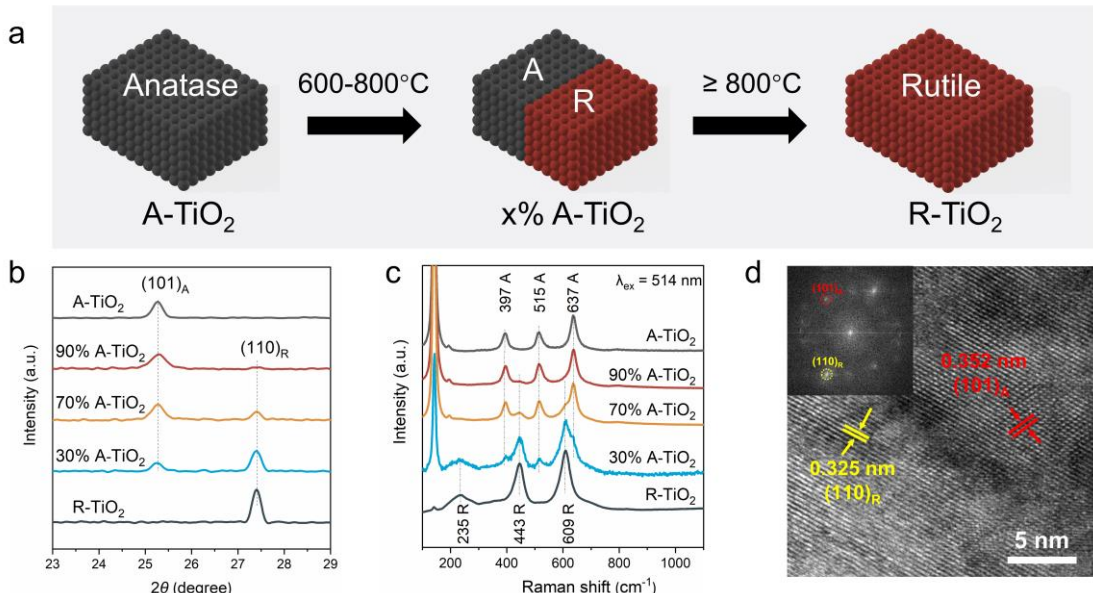
567 **Author contributions**

568 Y.J. and Z.T. conceived the idea, developed the outline, designed the experiment and compiled the
569 manuscript. Y.J. conducted all the experiments and tests with the assistance of W.Z., S.L., Y.F.,
570 F.W., X.Q., Y.Z., and Y.Z., C.L. coordinated the project and provided critical feedback. Z.T.
571 supervised the whole project.

572

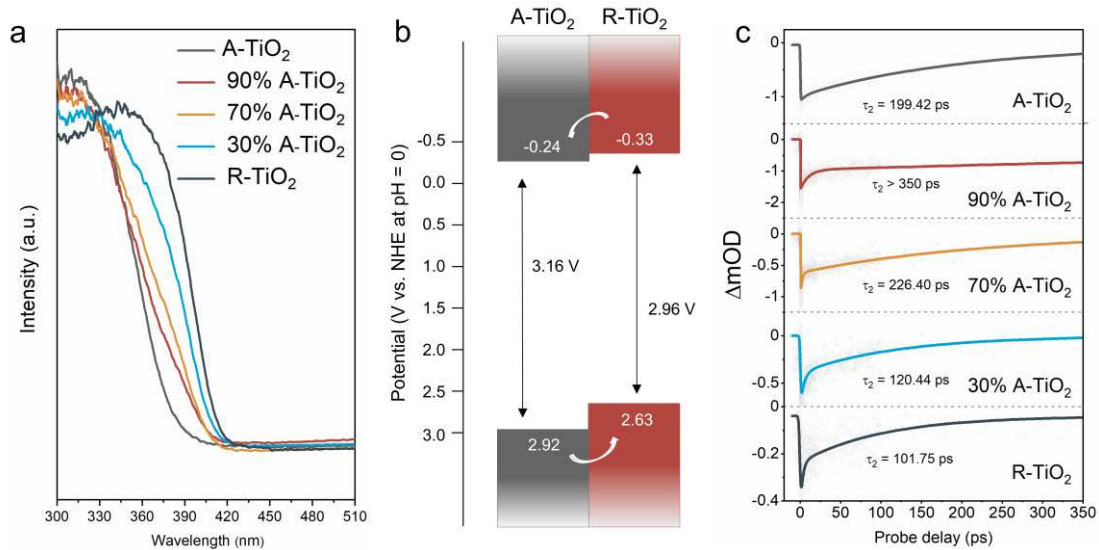
573 **Competing interests**

574 The authors declare no competing interests.

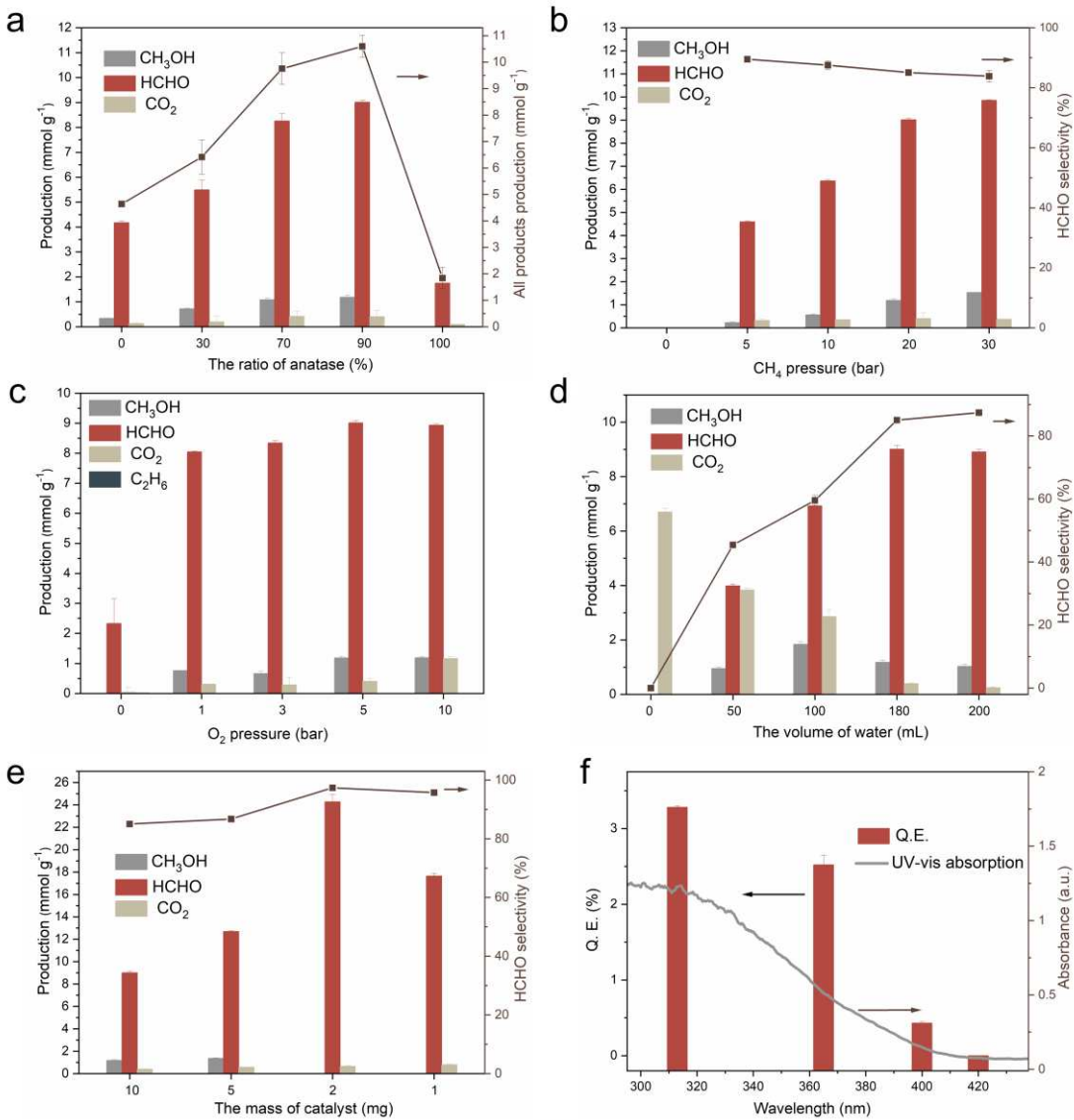


575
 576 **Fig. 1 | Synthesis and characterization of A/R-TiO₂.** (a) Scheme of phase transformation from
 577 Anatase to x% Anatase/Rutile and Rutile. (b) XRD patterns and
 578 (c) Raman spectra of A-TiO₂, x% A-TiO₂ and R-TiO₂ (from top to bottom). The Raman spectra are
 579 excited at 514 nm. (d) HRTEM image of A/R-TiO₂, and the inset is the corresponding fast Fourier
 580 transform (FFT) image.

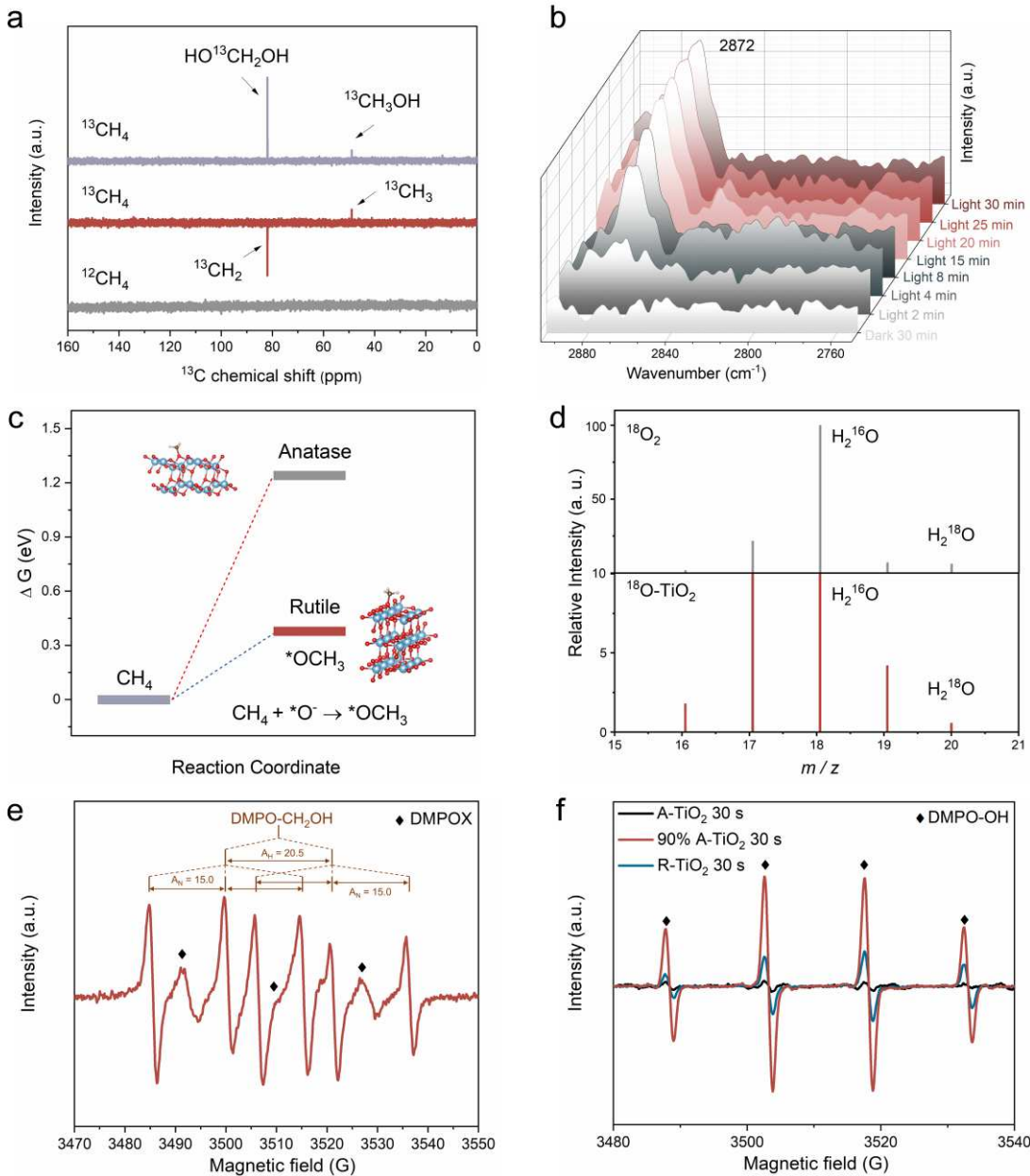
581



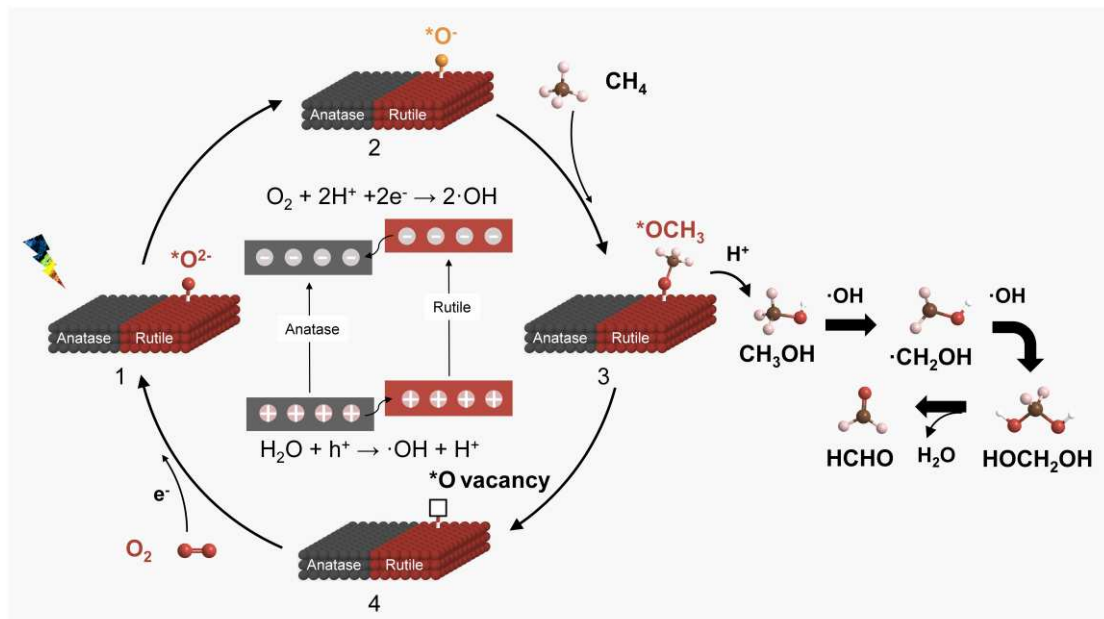
584 **Fig. 2 | Optical property and photogenerated carrier separation of A/R-TiO₂.** (a) UV-vis DRS
 585 of A-TiO₂, x% A-TiO₂ and R-TiO₂. (b) Scheme of charge transfer pathway between anatase phase
 586 and rutile phase in TiO₂. (c) Ultrafast transient absorption signal as a function of probe delay for
 587 A-TiO₂, x% A-TiO₂ and R-TiO₂ (probed at 600 nm). All the data are recorded with a 355 nm
 588 pump. Note that the time constant τ_2 given in the plot is derived from the exponential fitting of the
 589 relevant kinetic trace.



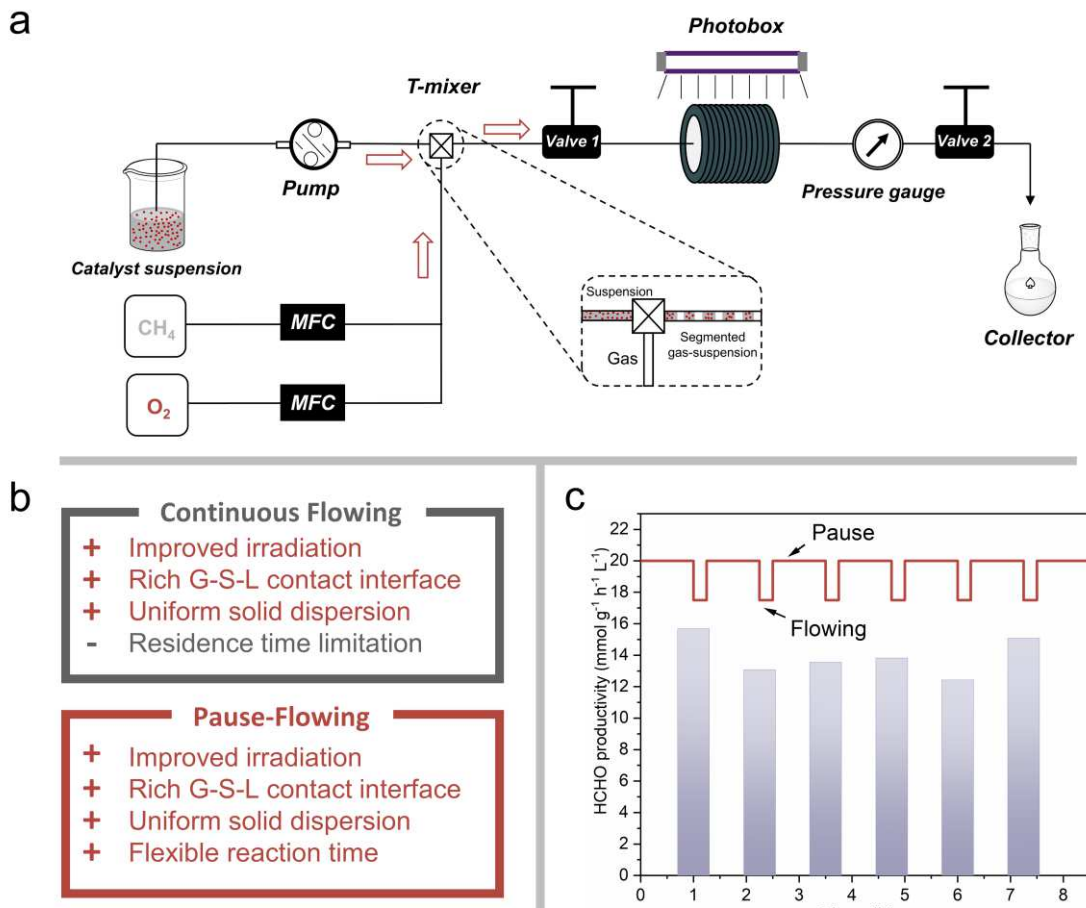
590
591 **Fig. 3 | Photocatalytic methane oxidation performance.** Production for oxygenates (a) using A-
592 TiO₂, x% A-TiO₂ and R-TiO₂ as photocatalysts, (b) at varied CH₄ pressures, (c) at varied O₂
593 pressures, (d) using different amounts of H₂O, (e) with different mass of catalyst. Reaction
594 conditions: 10 mg 90% A-TiO₂ (or other catalysts in (a)), 5 bar O₂, 20 bar CH₄, 180 mL H₂O, 3 h
595 reaction time, Xe lamp with wavelength range of 300 nm to 1100 nm and irradiation intensity of
596 130 mW cm⁻². Other condition variables are changed according to the parameters shown in the
597 figures. (f) QE values at varied monochromatic wavelengths along with UV-vis DRS of 90% A-
598 TiO₂. Error bars represent standard deviation (s.d.) with three independent experiments.



599
600 **Fig. 4 | Reaction mechanism of photocatalytic methane oxidation.** (a) ^{13}C CPD (top) and ^{13}C
601 DEPT-135 (middle) spectra of products from $^{13}\text{CH}_4$ oxidation. The contrast experiment shows
602 there are no detected signals from $^{12}\text{CH}_4$ oxidation (bottom). (b) *In situ* DRIFTS spectra of
603 photocatalytic CH_4 oxidation over 90% A-TiO₂. (c) Gibbs free energy of lattice O^- activated
604 methane to $*\text{OCH}_3$ on anatase (101) and rutile (110) surfaces, and corresponding calculation
605 models. Note that anatase (101) and rutile (110) are major exposed surfaces of A/R-TiO₂ discerned
606 by XRD patterns. (d) GC-MS spectra of H_2O from HCHO via acetylacetone color-developing
607 reaction. The HCHO is generated using $^{18}\text{O}_2$ or $^{18}\text{O}-\text{TiO}_2$. The m/z peaks at 18, 19 and 20 stand for
608 H_2^{16}O , $[\text{H}_2^{16}\text{O} + 1]^+$ and H_2^{18}O , respectively, and H_2^{16}O originates from solvent water. (e) ESR
609 spectra over 90% A-TiO₂ under light irradiation in methanol. (f) ESR spectra over A-TiO₂, 90% A-
610 TiO₂ and R-TiO₂ under light irradiation in water.
611



614 **Fig. 5 | Proposed mechanism of photocatalytic methane oxidation on A/R-TiO₂.** Scheme of
615 photocatalytic conversion of CH₄ to HCHO on A/R-TiO₂.
616



619 **Fig. 6 | Photocatalytic methane oxidation in “pause-flowing” reactor for scale-up application.**
620 (a) Scheme of “pause-flowing” reactor. MFC is abbreviation of mass flow controller. (b)
621 Comparison of “pause-flowing” reactor and conventional continuous flowing reactor. (c) Time-
622 dependent photocatalytic formaldehyde production over 90% A-TiO₂ in “pause-flowing” reactor
623 and the diagram of pause and flowing operation. Reaction conditions: 0.055 g/L 90% A-TiO₂ and
624 water suspension, 5 bar reaction pressure (CH₄/O₂ = 4/1), 15 min flowing time and 1 h pause time,
625 120 W 365 nm LED strip as light source.

Supplementary Files

This is a list of supplementary files associated with this preprint. Click to download.

- [Supplementaryinformation.pdf](#)